Noname manuscript No.
(will be inserted by the editor)

A systematic analysis of the XMM-Newton background: III. Impact of the magnetospheric environment.

Simona Ghizzardi[1] · **Martino Marelli**[1] · **David Salvetti**[1] · **Fabio Gastaldello**[1] · **Silvano Molendi**[1] · **Andrea De Luca**[1,3] · **Alberto Moretti**[2] · **Mariachiara Rossetti**[1] · **Andrea Tiengo**[1,3]

Received: date / Accepted: date

Abstract A detailed characterization of the particle induced background is fundamental for many of the scientific objectives of the Athena X-ray telescope, thus an adequate knowledge of the background that will be encountered by Athena is desirable. Current X-ray telescopes have shown that the intensity of the particle induced background can be highly variable. Different regions of the magnetosphere can have very different environmental conditions, which can, in principle, differently affect the particle induced background detected by the instruments. We present results concerning the influence of the magnetospheric environment on the background detected by EPIC instrument onboard XMM-Newton through the estimate of the variation of the in-Field-of-View background excess along the XMM-Newton orbit. An important contribution to the XMM background, which may affect the Athena background as well, comes from soft proton flares. Along with the flaring component a low-intensity component is also present. We find that both show modest variations in the different magnetozones and that the soft proton component shows a strong trend with the distance from Earth.

Keywords X-ray astrophysics · Instrumentation:background · Particle background · Radiation environment · Soft proton background

1 Introduction

The characterization of the background in X-ray observations is a major concern for astronomers interested in studying faint and diffuse sources. The Eu-

S. Ghizzardi
[1] INAF-IASF Milano, via E. Bassini 15, I-20133 Milano, Italy
E-mail: simona@iasf-milano.inaf.it

[2] INAF-Osservatorio Astronomico di Brera, via Brera 28, I-20121 Milano, Italy ·
[3] Istituto Universitario di Studi Superiori, piazza della Vittoria 15, I-27100 Pavia, Italy

ropean Photon Imaging Camera (EPIC) on board XMM-Newton does not provide an exception to this situation. Its instrumental background can be divided into electronic noise and particle-induced background (see [3] for a detailed description). The latter component has two main contributions: an "unfocused" component, caused by high-energy particles ($E >$ MeV) which are able to reach also the unexposed regions of the field-of-view (FOV) and and a "focused" component, which causes an excess of signal only in the part of the FOV exposed to the sky and is usually associated to the so called "soft protons". These low-energy particles (a few tens of keV) are somewhat focused by the telescope and do not produce signal in the unexposed corners of the FOV. When the satellite encounters in its orbit a cloud of such particles a sudden and highly variable count-rate excess is detected ("soft proton flares"), which hampers the scientific exploitation of the data. These particles are likely accelerated in the Earth magnetosphere and therefore the intensity of the particle induced background may depend on the magnetospheric environment during the observations. The orbit of XMM-Newton is highly elliptical (with an apogee of about 115,000 km and a perigee of about 6,000 km from Earth) and crosses regions of the magnetosphere with different properties in terms of strength and orientation of the magnetic field, speed and density of the particles etc. It goes from the radiation belts near the perigee, through the magnetoplasma and magnetotail, to the magnetosheath and eventually out of the bow shock into the solar wind. XMM-Newton data are therefore very useful to test the dependence of the induced particle background in different magnetospheric environments.

This work is part of a wider project that aims to characterize the effects of focused and unfocused particles on X-ray detectors through the analysis of XMM-Newton data. In this paper we focus on the impact of the magnetospheric enviroment on the XMM-Newton background components that cause an excess count rate in-the-field-of-view (*inFOV*) with respect to the unexposed corners (focused background component; *outFOV*). Hence to investigate and quantify the background we make use of the difference *inFOV*-*outFOV* rate (see Sec 4.1). Complementary results are presented in companion papers: details about the data reduction, cleaning and filtering are provided in [1]; in [2] we provide a characterization of the focused background component. Finally in [3] we present results about the origin of the unfocused particle background and about the focused soft protons background. This work has been developed within the AREMBES[1] (Athena Radiation Environment Models and X-ray Background Effects Simulators) project, a ESA R&D Activity. The data sample construction and reduction has been performed thanks to the synergy with EXTraS[2] (Exploring the X-ray Transient and variable Sky; [4]), a EU-FP7 project.

[1] http://space-env.esa.int/index.php/news-reader/items/AREMBES.html
[2] http://www.extras-fp7.eu

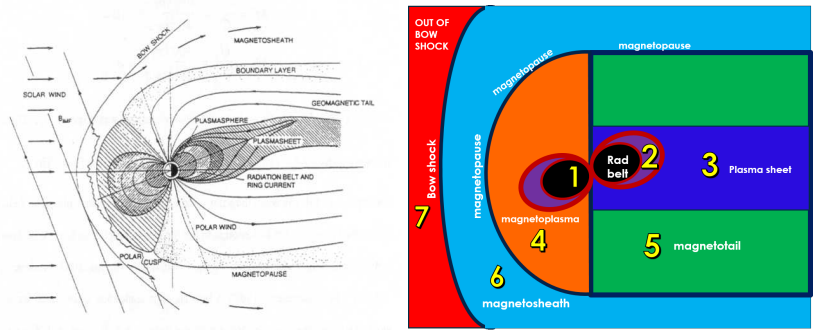

Fig. 1: A schematic view of the magnetosphere of the Earth (left panel) and our simplified division of the magnetosphere into 7 magneto-zones (right panel). The color code represented here will be adopted throughout the paper.

2 The dataset

We adopt the largest XMM-Newton data set ever analysed based on the entire XMM-Newton archive. It collects $\sim$ 100Msec of data from observations performed between 2000-2012 (revolution 35 to 2330). The description of the sample and the reduction and cleaning procedures are provided in [1]. In addition, we reject periods that are classified as "SEP contaminated" to avoid eventual unwanted biases; the list of all the SEP contaminated periods is provided by the ESA Solar Energetic Particle Environment Modelling (SEPEM) application server[3]. After the removal of the time intervals affected by SEP events, the sample reduces to 87.8 Msec of cleaned data.

3 Method

3.1 Partition of the magnetosphere into magneto-zones

The terrestrial magnetosphere prevents most of the solar wind from hitting the Earth, although some energetic particles can enter it. In Figure 1 (left panel), we provide a schematic representation of the Earth magnetosphere.

The outermost layer of the magnetosphere is the bow shock; it forms when the supersonic solar wind encounters the Earth magnetic field. The solar wind across the bow shock surface is then heated up and slowed down by the Earth's magnetic field which acts like an obstacle. As a consequence, the solar wind starts flowing around the obstacle forming the magnetopause, a surface which divides the terrestrial magnetic field from the solar wind that flows around it.

We adopt a simplified characterization of the Earth magnetosphere (see Figure 1, right panel) and divided the magnetosphere into 7 typical magneto-

[3] http://dev.sepem.oma.be/help/event_ref.html

zones. The Van Allen radiation belts are modeled through the L-shell model by [5] $R = L\cos 2\lambda$, where: R is the radial coordinate of the field line in units of Earth radii ($R_E = 6371$km); λ is the magnetic latitude and the L-shell parameter is $L = R_0/R_E$; R_0 is the intersection of the field line with the geomagnetic Equator. Variables are defined in the geocentric solar magnetospheric system (GSM). Since the external boundary of the radiation belts is highly variable, we split this region into two different zones: the "radiation belts" (#1) inside the $L = 4$ shell and the "radiation belts exit" (#2): the region between $L = 4$ and $L = 6$ where the satellite exits the belts and enters the outer magnetospheric ambient. The plasma sheet (#3) is assumed to be a cylindric region centered on the Earth-Sun line, with the axis parallel to the ecliptic plane in the anti-Sunward direction, with radius $R = 5R_E$ [6].

Inside the magnetopause, the magnetic field lines have a different shape on the nightside and dayside regions. In the dayside region, magnetic field lines are closed, distorted and compressed by the pressure of the solar wind. Conversely, in the nightside regions the magnetic field lines are stretched and open. We divide the area inside the magnetopause into two different sectors: the anti-Sunward region is known as magnetotail (#5) and we dub "magnetoplasma" the Sunward zone (#4). To model these regions, we use a simple model [7] for the magnetopause radius in the dayside direction

$$R_{MP} = \frac{14.21}{1 + 0.42\cos\theta} \tag{1}$$

where the distance R_{MP} is in R_E units and θ is the angle from the Earth-Sun line. Coordinates are in the geocentric solar ecliptic (GSE) system. On the nightside, we assume the magnetopause to be a cylindrical surface, with radius $R = 14.21R_E$, with the cylinder axis parallel to the ecliptic plane and centered on the Earth-Sun line.

The magnetosheath (labelled as #6) is the plasma region between the bow shock and the magnetopause in which the shocked solar wind is heated and slowed down from supersonic to subsonic speeds. The boundaries for this magneto-zone are the magnetopause surface and the bow shock surface that we model following [7]:

$$R_{BS} = \frac{22.74}{1 + 0.75\cos\theta} \tag{2}$$

where the distance R_{BS} is in R_E units and θ is the angle from the Earth-Sun line.

We finally label as magneto-zone #7, the regions out of the bow shock when the satellite is outside the magnetosphere and embedded in the solar wind.

The description used in our analysis for the magnetosphere is clearly simplified and the model neglects possible time variations of the shape and boundaries of the magneto-zones: solar wind speed and pressure vary with time and eventually compress the magnetopause and bow shock surfaces changing their boundaries. It should also be noted that region boundaries are not sharp edges

and these zones are not strictly distinct, instead there may be smooth transitions from one region to another. However, also thanks to the very large quantity of data available, this simple description of the magnetosphere is appropriate to study in a statistical way how the various magnetospheric conditions can affect the XMM particle background.

3.2 XMM-Newton orbit segmentation

Our sample includes data from revolution 35 to 2330. For each revolution, we derive the XMM-Newton orbit and divide it into segments according to the magnetosphere environment crossed while travelling. Then, for each revolution and for each magneto-zone we find the Good Time Intervals (GTI) that can be used to filter the sample data and analyze the background region by region. In Figure 2 we plot, as an example, a 3D representation of the XMM-Newton orbits during revolution 1016 (26-27 June 2005) and revolution 1466 (10-11 December 2007). Closed lines around the Earth track the torus of the radiation belts whose orientation varies in time due to seasonal and daily motion of the Earth's dipole tilt angle. To derive magnetic axis inclination changes, we use the SolarSoftware (SSW) IDL package [8], where the dipole axis position is calculated according to the International Geomagnetic Reference Frame (IGRF) model, as described in [9]. The plasma sheet cylinder is represented through a series of red circles, extending in the anti-Sun side; black and blue dashed lines reproduce the magnetopause and the bow shock surface respectively.

The orbit segments are plotted using the color code defined in Figure 1 and the orbit parts where EXTraS data are available are plotted with a thick line. EXTraS data generally cover only a fraction of the orbit. The lack of data during the revolution can be due to various reasons. First of all, EPIC cameras are closed at low altitudes to avoid damage from exposure to soft protons during the passages through the radiation belts: XMM has a minimum observation altitude of 40,000 km. This is responsible of missing data at the beginning and at the end of each orbit. Observations can be missing for corrupted or bad data or could have been rejected from the EXTraS archive [2]. In addition, gaps are present during slew transitions from an observation target to another. The portions of the orbits where EXTraS data are not available have been reconstructed using the information available in the Radiation Monitor page of the XMM-Newton website[4] where fits files containing orbit parameters can be retrieved. In these files, the XMM-Newton orbit status is stored with a 1 second cadence and their processing can be very time-consuming. When available, we used Trend Data in HEASARC[5], as they provide XMM orbit parameters with a 64 sec cadence. We thus use Radiation Monitor orbit files only when Trend Data are missing.

XMM-Newton spends most of the time south of the ecliptic plane. The direction of the orbit and the apogee position change during the year. De-

[4] http://www.cosmos.esa.int/web/xmm-newton/list-of-tc-radmon

[5] https://heasarc.gsfc.nasa.gov/docs/xmm/xmmhp_trend.html

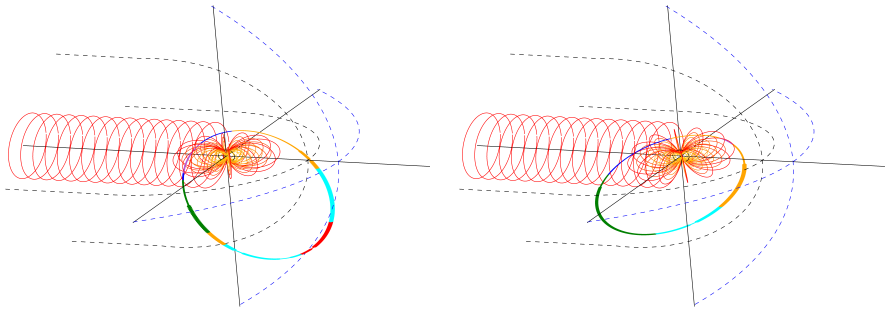

Fig. 2: XMM-Newton orbit for revolution 1016 (left panel) and 1466 (right panel). The coordinate grid is in Geocentric Solar Ecliptic (GSE) coordinate system, with the Earth in the origin and the Sun located at the end of the X-axis at the right-side of the plot; XY plane is the ecliptic plane. Radiation belts (closed lines arount the Earth) are plotted for L in the range $L = 2$(yellow) to $L = 6$(red) with colors with orange tones for intermediate values of L. Red cicle mark the plasma sheet and black and blue dashed lines are the projection of the magnetopause and bow shock surface respectively. The XMM-Newton orbit segments are plotted using the color codes defined in Figure 1.

pending on the season, the orbit extends toward the Sun, with the apogee eventually exiting the bow shock surface (like in the left panel of Figure 2) or in the anti-Sun direction, keeping completely inside the magnetotail and the magnetosheath (right panel of Figure 2).

In Figure 3 (left panel) we plot the full lightcurve of the whole EXTraS sample, with colors marking the different magneto-zones. In the first observation years, the out-of-bow-shock region (in red) is periodically reached during the summer periods. Successively, namely after July 2005, the satellite is no more able to reach this region, due to a gradual circularization of the orbit and to variations of its inclination angle.

During the 13 years under analysis XMM recursively crosses all the magneto-zones. The fraction of time spent in each ambient depends on the orbit geometry and inclination and on the extension of each zone. In Table 1 we report the time (and fraction) spent in each magneto-zone and the corresponding amount of EXTraS data. Particularly interesting is the out-of-bow-shock region (#7), where the satellite is out of the Earth magnetosphere. bf This region is of particular interest as it should be mostly free of background components produced within the magnetosphere. XMM-Newton spent in the out-of-bow-shock zone only 3.2% of the time with 3.7 Msec of EXTraS data in this region. Most of the time is spent into the magnetosheath and the magnetotail. Little time is

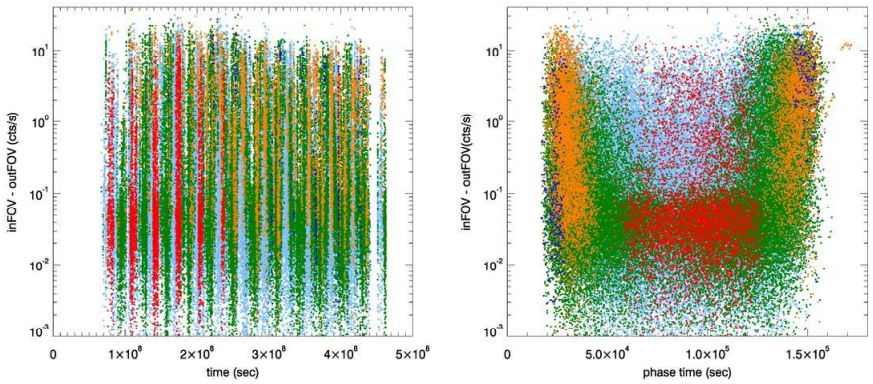

Fig. 3: Background intensity (*inFOV-outFOV* rate, see Sec. 4.1) in the whole EXTraS sample versus time (left panel) and orbit phase (right). For each orbit, the phase time is the time measured starting from the beginning of the orbit. The orbit is assumed to start at perigee. Colors mark the different magneto-zones following the color codes of Figure 1

Table 1: We report the total time (and the corresponding fractional value) spent by XMM-Newton in the different magnetospheric zones. We show both the time scored by the Radiation Monitor (which roughly corresponds to the total time effectively spent in each region) and the total time (with the corresponding fractional value) of EXTraS data available in the same region.

Magneto-zone	Radiation Monitor		EXTraS Archive	
	Time (Msec)	Fraction (%)	Time (Msec)	Fraction (%)
#1 Radiation belts	3.3	0.9	0.0	0.0
#2 Radiation belts exiting	13.2	3.4	0.0	0.0
#3 Plasma sheet	20.3	5.2	0.4	0.5
#4 Magnetoplasma	58.4	15.0	5.1	5.8
#5 Magnetotail	126.1	32.5	35.6	40.5
#6 Magnetosheath	154.7	39.8	43.0	49.0
#7 Out of bow shock	12.4	3.2	3.7	4.2

spent into the plasma sheet. Because of its position (in the nightside and along the ecliptic plane) and its thinness, the plasma sheet hosts the satellite only for about 5% of the time with only 5 Msec of data available. Due to required off time near the perigee, no data are available in regions #1 and #2. These two magnetospheric regions will not be discussed further in this paper.

4 Results

4.1 XMM-Newton background rate and magnetospheric environment

As anticipated in Sec. 1, we use the *inFOV-outFOV* rate to estimate the EPIC background, i.e. the difference between the count rate measured in the area where X-ray photons are focused (*inFOV*) and the count rate measured in the unexposed areas (*outFOV*) of the detector. Starting from the lightcurve of the whole EXTraS sample, we derived the *inFOV-outFOV* rate versus the orbit phase (Figure 3, right panel); each orbit lightcurve is plotted versus the time elapsed from the perigee position. This provides a qualitative picture of the EPIC *inFOV* excess background along the orbit. Many events feature a high (say $\gtrsim 0.1$ cts/s) *inFOV-outFOV* rate which can occasionally rise up to ~ 200 cts/s; these correspond to soft proton flares. However, the bulk of the data lies in the range $[0.01 - 0.1]$ cts/s where the low-intensity component of the background dominates. A full comprehension of the origin of both the soft proton flares and of the low-intensity component is still lacking. Soft proton flares can include components having different origins: solar energetic particles events (SEP) or particles generated at the bow shock or inside the magnetosphere (e.g. in the radiation belts). A more detailed discussion about this issue is provided in [3]. The nature of the low-intensity component is still unclear: as discussed in [2], it is probably not associated to soft protons and may be due to Compton interaction of hard X-ray photons with the detector.

Since the perigee is the starting (and ending) point of the orbit, at the center of the plot we find the events recorded at the apogee: here are concentrated the "out of bow shock" data (in red). Apparently, the *inFOV-outFOV* rate here is slightly lower than in the other regions, with a lower spread of data, although not free from soft protons flare events. Blue and orange dots, respectively labeling the plasma sheet and the magnetoplasma on the dayside, are located at the edges of the plot near the perigee at the beginning and at the end of the orbit. Indeed, the satellite lies in these areas just after exiting (or before entering) the radiation belts. The *inFOV-outFOV* rate in these regions seems on average larger than elsewhere and the quantity of data in this region is low since the time spent in the plasmasheet and into the magnetoplasma is only 0.4 Msec and 5 Msec. Hence, Figure 3 (right panel) provides two relevant results: 1) the presence of soft proton flares is not related to any particular magnetozone, and they are distributed throughout all the different regions, 2) no portion of the orbit is free from soft proton flares.

To quantify the variation of the *inFOV* background excess in the different magnetospheric ambients we plot, in Figure 4, the distributions of *inFOV-outFOV* rate for the five considered zones: distributions on the left column are zoomed to low *inFOV-outFOV* values (0.1-0.3 counts/s) for a better visualization of the low-intensity component, while the wider range is used in the panel on the right column to better inspect the tail extension. The distributions show the presence of two main contributions, confirming the qualitative picture provided by Figure 3: 1) the peaked Gaussian-like distribution at low

Table 2: Gaussian peak positions obtained fitting *inFOV-outFOV* rate; flaring mean rate (*inFOV-outFOV* > 0.1) for each magnetozone.

Magneto-zone	Gaussian Peak cts/s	Flaring mean rate (*inFOV-outFOV* > 0.1) cts/s
#3 Plasma sheet	0.014±0.003	4.075±0.233
#4 Magnetoplasma	0.039±0.001	2.425±0.037
#5 Magnetotail	0.0179±0.0001	1.700±0.020
#6 Magnetosheath	0.0165±0.0001	1.544±0.015
#7 Out-of-bow-shock	0.0168±0.0002	1.522±0.048

count rates describes the low-intensity component where the bulk of the data lies; 2) all the distributions feature a long tail toward high count rate values, representing the flaring component. The wide extension of the tail is a symptom of the importance of the flaring component, which, in all the magnetospheric regions, accounts for a notable fraction of events: indeed the fraction of time when the background is affected by soft protons flares is $\gtrsim 30\% - 40\%$ (see [2]). Following [2] we fit the distributions using a Gaussian function in addition to a modified Lorentzian distribution $F(x)$ defined:

$$F(x) = \frac{LN x^{\Gamma_1}}{1 + \left|\frac{2(x-LC)}{LW}\right|^{\Gamma_2}} e^{-x/X_0} \tag{3}$$

where LN, LC and LW are the normalization, the center and the width of the Lorentzian component; X_0 is the exponential cut-off and Γ_1, Γ_2 are the two slopes. The best fit functions for each magnetozone are overplotted in Figure 4. We stress that the adopted model is purely phenomenological and there exists a strong correlation between the parameters. This requires that we consider uncertainties on model parameters with some caution.

The Gaussian peak derived from the fitting procedure is suitable to quantify the low-intensity component contribution in the different magnetospheric ambients.

Best fit values for each magnetozone are reported in Table 2 (second column).

We note that peak positions show very modest variations from a zone to another as far as the three external zones (#5, #6, and #7 which contain most of the data) are concerned: for these regions the magnetic environment has a modest influence on the *inFOV* background excess. The statistics in region #3 (plasmasheet) is very low and the obtained curve hosts some artificial features that the fitting procedure introduces to follow distribution irregularities. Best-fit values for this region, albeit with small error bars, are not reliable from a physical point of view and we cannot use them to draw any conclusion. The region #4 features a higher best-fit value for the peak. However in this region the contribution of the flaring component is higher and it becomes comparable to the low-intensity component, inducing a possible bias on the inference of the best-fit value for the Gaussian peak. It is impossible to disentangle the

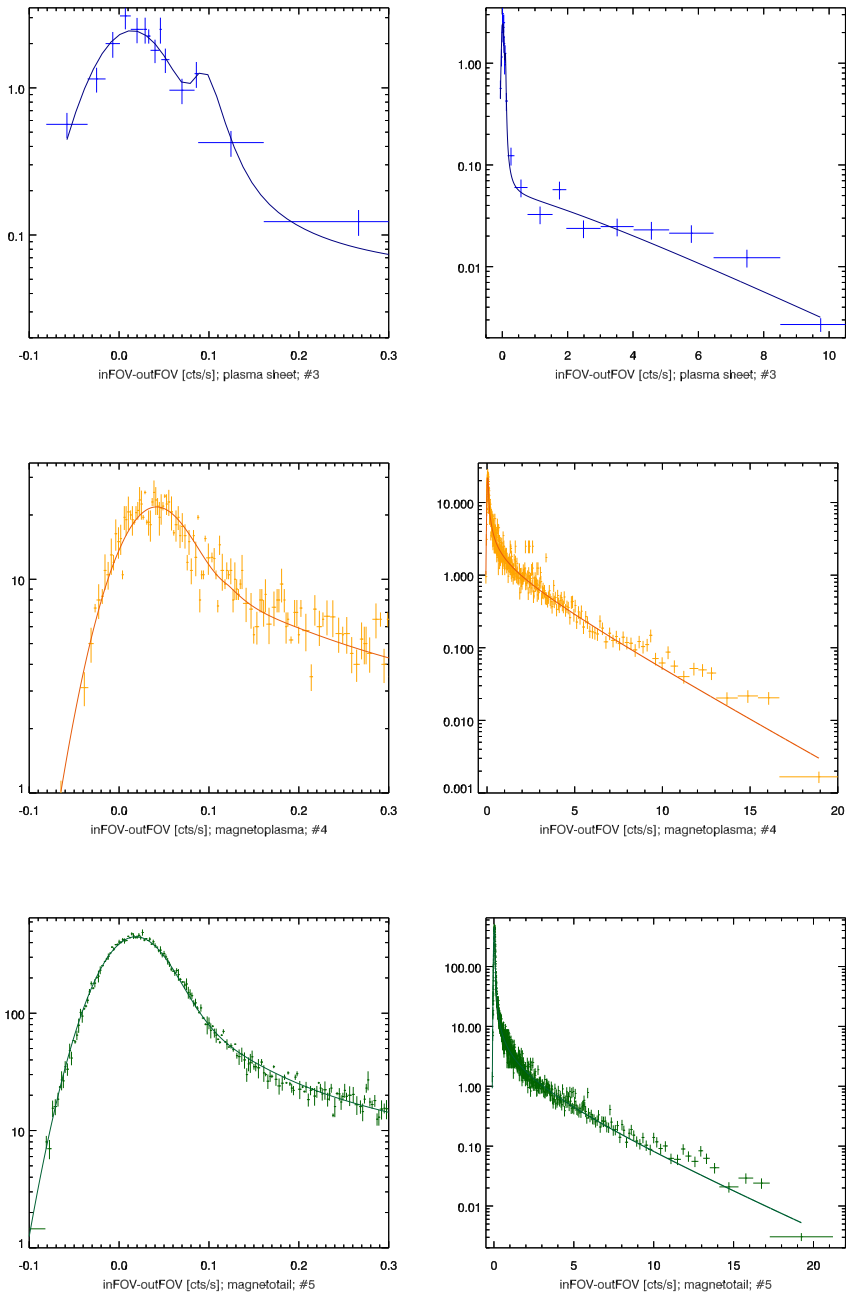

Fig. 4: *inFOV-outFOV* distributions of all the magnetozones. Distributions in the left column are zoomed in the range [-0.1,0.3] for a better visualization of the low-intensity component. Best fit functions (see text) are overplotted. Different regions are color coded as in Figure 1. (Continues in next page)

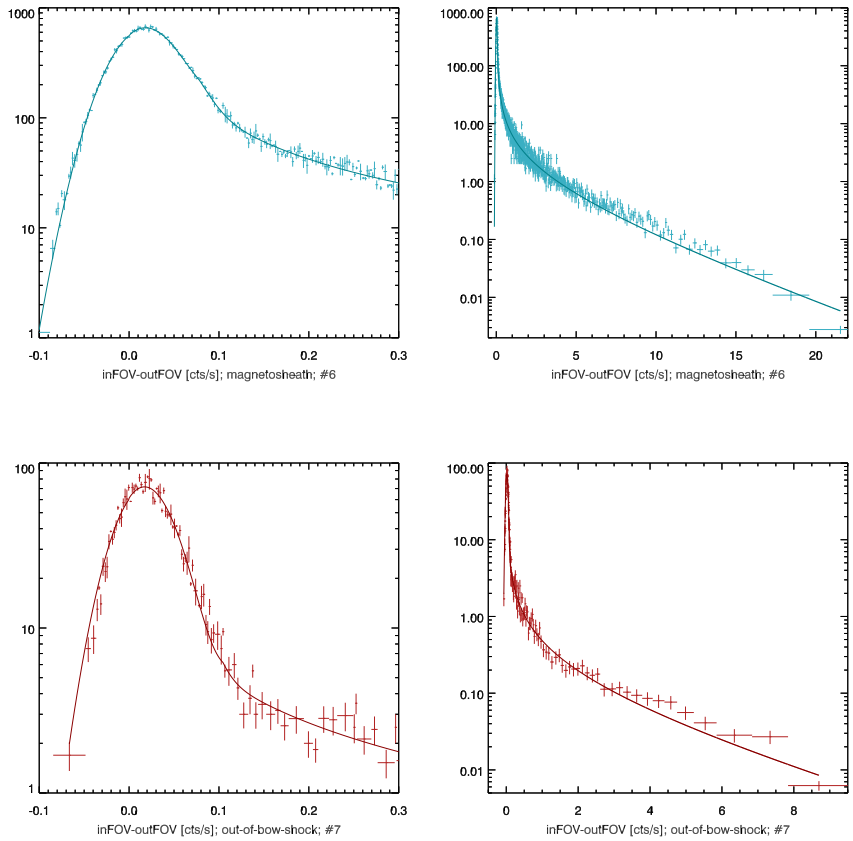

Fig. 4: (...continued) *inFOV-outFOV* distributions of all the magnetozones. Distributions in the left column are zoomed in the range [-0.1,0.3] for a better visualization of the low-intensity component. Best fit functions (see text) are overplotted. Different regions are color coded as in Figure 1.

contamination of the tail on the peak position from a possible real shift of the low-intensity component; thus the behavior of the low-intensity component in this region is not easily interpreted.

While the best fit of the gaussian peak is a suitable parameter to describe the low-intensity component, the best-fit parameters of the Lorentzian function are not good indicators to quantify the intensity of the flaring component. A suitable indicator is provided by the mean of the high-rate-component: we choose as fiducial threshold 0.1 cts/s and we calculate the mean value of the *inFOV-outFOV* rate above this threshold and we refer to it as the flaring mean rate. The values of the flaring mean rate for each magnetozone are reported

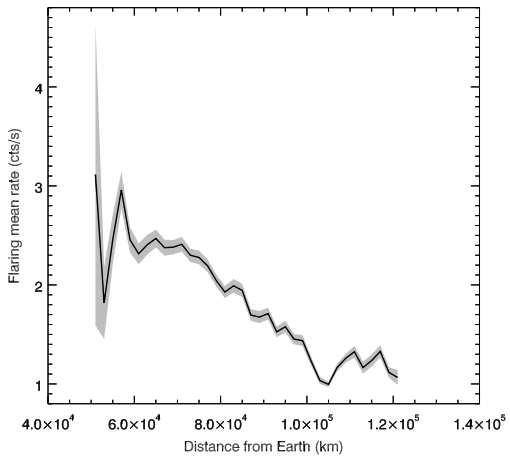

Fig. 5: Mean for the *inFOV-outFOV* rate, for count rates > 0.1 cts/s, of the whole sample as a function of the XMM- Newton distance from the Earth.

in Table 2 (third column). The flaring mean rates show moderate variations when regions #5, #6 and #7 are concerned, with the out-of-bow-shock region featuring the lowest value, though very similar to the other two values. Regions #3 and #4 feature higher values.

4.2 Soft protons flares and XMM-Newton altitude

The results reported in the previous section show that the flaring component exhibits modest variations in the various magnetozones, with magnetoplasma and plasmasheet (which are located in the innermost regions, close to the radiation belts) featuring the highest values, while the out-of-bow-shock region records the smallest values. This suggests that the *inFOV-outFOV* flux may be related to the altitude of the satellite rather than to the particular magnetozone.

To inspect in detail the *inFOV-outFOV* behavior at different altitudes, we rebinned data using 2-km-wide bins. The behavior of the low-intensity component cannot be studied through 2-km-wide shells, since statistics is not enough to perform the fitting procedure. The study of this component requires a specific and extensive analysis that is beyond the aim of this article and will be addressed in a forthcoming paper. For the following discussion we restrict the analysis to the flaring component. We determined in each bin the mean of the *inFOV-outFOV* rate (for count rates > 0.1 cts/sec, i.e. the flaring mean rate), irrespective of the magnetospheric environment. In Figure 5 we plot this indicator as a function of the XMM-Newton distance from the Earth. The flaring mean rate significantly decreases with the distance: this means that

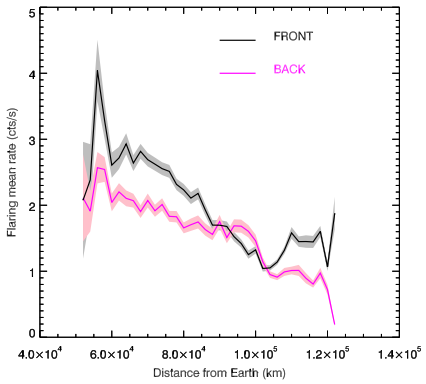

Fig. 6: Mean for the *inFOV-outFOV* rate (for count rates > 0.1 cts/s) as a function of distance from Earth in the dayside (black) and in the nightside (magenta) of the magnetosphere.

soft proton flares affect the XMM-Newton background at low altitudes more than at high altitudes, even though the flaring mean rate never drops below 1 cts/s, showing that this background component can occur in all parts of the XMM-Newton orbit.

4.3 Soft protons rate Sunward and anti-Sunward

A further important check concerns the possible differences in the *inFOV-outFOV* rate due to the position of XMM-Newton in the dayside or in the nightside of the magnetosphere. As mentioned in the previous section, the procedure cannot be applied to the low intensity component and we focus on the soft proton flares component. In order to understand if the front/back position with respect to the Sun can be a discriminatory factor, we evaluate the mean of the *inFOV-outFOV* rate (for count rates > 0.1 cts/sec) in the same 2-km-wide shells used in Figure 5, and separate regions Sunward and anti-Sunward. The two profiles are plotted in Figure 6. Both in the dayside and nightside of the magnetosphere the flaring component features a decrease with the altitude. In general, data taken in the dayside have a higher value than data taken in the nightside. This suggests that regions in the backside of the magnetosphere are less contaminated by soft-proton-flares than regions in the dayside, with little influence from the magnetospheric environment.

5 Conclusions

In this work we studied the role played by the different magnetospheric ambients on the *inFOV* excess background (*inFOV-outFOV* rate) detected by

XMM-Newton. Two main components contribute to the background: a low-intensity component (with rate $\lesssim 0.1$ cts/s) and a soft proton flaring component (with rate $\gtrsim 0.1$ cts/s). Our analysis shows that moving from a magnetozone to another has a moderate influence both on the low-intensity background and flaring soft proton component. On the contrary, the soft proton rate is highly related to the satellite altitude with higher rates at low altitudes. A substantial difference in the soft proton rate is found when comparing Sunward with anti-Sunward regions, the former featuring a higher background rate than the latter.

Acknowledgements The AHEAD project (grant agreement n. 654215) which is part of the EU-H2020 programm is acknowledged for partial support. This work is part of the AREMBES WP1 activity funded by ESA through contract No. 4000116655/16/NL/BW. Results presented here are based, in part, upon work funded through the European Union Seventh Framework Programme (FP7-SPACE-2013-1), under grant agreement n. 607452, "Exploring the X-ray Transient and variable Sky - EXTraS".

References

1. M. Marelli, D. Salvetti, F. Gastaldello, S. Ghizzardi, S. Molendi, A. De Luca, A. Moretti, M. Rossetti, A. Tiengo, *ExA submitted* (2017)
2. D. Salvetti, M. Marelli, F. Gastaldello, S. Ghizzardi, S. Molendi, A. De Luca, A. Moretti, M. Rossetti, A. Tiengo, *ExA submitted* (2017)
3. F. Gastaldello, S. Ghizzardi, M. Marelli, D. Salvetti, S. Molendi, A. De Luca, A. Moretti, M. Rossetti, A. Tiengo, *ExA submitted* (2017)
4. A. De Luca, EXTraS Collaboration, in *Exploring the Hot and Energetic Universe: The first scientific conference dedicated to the Athena X-ray observatory*, ed. by M. Ehle (2015), p. 55
5. C.E. McIlwain, JGR **66**, 3681 (1961). DOI 10.1029/JZ066i011p03681
6. L. Rosenqvist, A. Hilgers, E. Daly, H. Evans, Journal of Atmospheric and Solar-Terrestrial Physics **64**, 721 (2002). DOI 10.1016/S1364-6826(02)00033-0
7. K.D. Kuntz, S.L. Snowden, A&A, **478**, 575 (2008). DOI 10.1051/0004-6361:20077912
8. S.L. Freeland, B.N. Handy, Sol. Phys., **182**, 497 (1998). DOI 10.1023/A:1005038224881
9. M. Fränz, D. Harper, Planet. Space Sci., **50**, 217 (2002). DOI 10.1016/S0032-0633(01)00119-2